

Planetesimals Around Stars with *TESS* (PAST): I. Transient Dimming of a Binary Solar Analog at the End of the Planet Accretion Era

Gaidos, E.,^{1,2*} T. Jacobs,³ D. LaCourse,⁴ A. Vanderburg,⁵ S. Rappaport,⁶ T. Berger,^{7,2} L. Pearce,⁵ A. W. Mann,⁸ L. Weiss,^{7,9,2} B. Fulton,¹⁰ A. Behmard,¹¹ A. W. Howard,¹⁰ M. Ansdell,^{12,13} G. R. Ricker,¹⁴ R. K. Vanderspek,¹⁴ D. W. Latham,¹⁵ S. Seager,^{14,16,17} J. N. Winn¹⁸ and J. M. Jenkins¹⁹

¹Department of Earth Sciences, University of Hawai‘i at Mānoa, Honolulu, HI 96822, USA

²Kavli Institute for Theoretical Physics, UC Santa Barbara, Santa Barbara, CA 93106

³12812 SE 69th Place Bellevue, WA 98006, USA

⁴7507 52nd Place NE Marysville, WA 98270, USA

⁵Department of Physics, Kavli Institute for Astrophysics and Space Research, M.I.T., Cambridge, MA 02139, USA

⁶Department of Astronomy, The University of Texas at Austin, 2515 Speedway, Stop C1400, Austin, TX 78712, USA

⁷Institute for Astronomy, University of Hawaii at Mānoa, Honolulu, HI 96822, USA

⁸Department of Physics and Astronomy, University of North Carolina at Chapel Hill, Chapel Hill, NC 27599-3255, USA

⁹Parrent Fellow

¹⁰Department of Astronomy, California Institute of Technology, 1200 East California Boulevard, Pasadena, CA 91125, USA

¹¹Division of Geological and Planetary Sciences, California Institute of Technology, Pasadena, CA 91125, USA

¹²Center for Integrative Planetary Science, University of California at Berkeley, Berkeley, CA 94720, USA

¹³Department of Astronomy, University of California at Berkeley, Berkeley, CA 94720, USA

¹⁴Department of Physics and Kavli Institute for Astrophysics and Space Research, MIT, Cambridge, MA 02139, USA

¹⁵Center for Astrophysics | Harvard & Smithsonian, 60 Garden Street, Cambridge, MA 02138, USA

¹⁶Department of Earth, Atmospheric, and Planetary Sciences, MIT, Cambridge, MA 02139, USA

¹⁷Department of Aeronautical and Astronautical Engineering, MIT, Cambridge, MA 02139, USA

¹⁸Department of Astrophysical Sciences, Princeton University, Princeton, NJ 08544, USA

¹⁹NASA Ames Research Center, Moffett Field, CA 94035, USA

Accepted XXX. Received YYY; in original form ZZZ

ABSTRACT

We report detection of quasi-periodic (1.5-day) dimming of HD 240779, the solar-mass primary in a 5" visual binary (also TIC 284730577), by the *Transiting Exoplanet Survey Satellite*. This dimming, as has been shown for other “dipper” stars, is likely due to occultation by circumstellar dust. The barycentric space motion, lithium abundance, rotation, and chromospheric emission of the stars in this system point to an age of ≈ 125 Myr, and possible membership in the AB Doradus moving group. As such it occupies an important but poorly explored intermediate regime of stars with transient dimming between young stellar objects in star forming regions and main sequence stars, and between UX Orionis-type Ae/Be stars and M-type “dippers”. HD 240779, but not its companion BD+10 714B, has *WISE*-detected excess infrared emission at 12 and 22 μm indicative of circumstellar dust. We propose that infrared emission is produced by collisions of planetesimals during clearing of a residual disk at the end of rocky planet formation, and that quasi-periodic dimming is produced by the rapid disintegration of a $\gtrsim 100$ km planetesimal near the silicate evaporation radius. Further studies of this and similar systems will illuminate a poorly understood final phase of rocky planet formation like that which produced the inner Solar System.

Key words: stars: binaries – kinematics and dynamics – circumstellar matter – planetary systems – planet-star interactions – planets & satellites: protoplanetary disks

1 INTRODUCTION

Observations of $\lesssim 10$ Myr-old Young Stellar Objects (YSOs) are a window into the past of the Solar System, as well as the thousands of planetary systems around main sequence stars revealed by space-based transit surveys, especially *Kepler*, and ground-based radial velocity surveys. YSOs, including the low-mass T Tauri stars, were first identified by their variability (Joy 1945), which remains a defining characteristic. This variability is a result of the rotation of a spotted photosphere, flaring, episodic accretion, but also transient obscuration of the star by circumstellar matter (dust). Variable Herbig Ae/Be stars were classified according to the behavior of their light curves (Herbst et al. 1994); “Type III” variables, represented by the archetype UX Orionis, exhibit deep photometric minima that last weeks to months and occur episodically on timescales of years. Such variables are readily identified and studied from the ground; changes in polarization and apparent color during dimming events indicate that dust, perhaps associated with the disk, are responsible for the obscuration (Natta et al. 1997). AA Tau, a T Tauri-type YSO, hinted at more diverse photometric variability among a wider range of stellar masses (Bouvier et al. 1999). AA Tau exhibited periodic (8.3 day) dimming until suddenly fading in 2013, behavior explained as obscuration by dust in a non-axisymmetric or “funnel” accretion structure orbiting interior to the inner edge of a disk that is truncated and warped by the star’s misaligned magnetic field (Bouvier et al. 2014). The dramatic, evolving variability of another T Tauri-type binary KH 15D is thought to be due to eclipses of one star by the precessing accretion disk of the other (e.g., Herbst et al. 2010).

Space-based photometry of star-forming regions by *CoRoT* and *Spitzer*, unimpeded by Earth’s rotation and atmosphere, led to identification of additional types of behavior, most notably “dipper” stars with episodic transient dimming lasting for a fraction of day (Alencar et al. 2010; Morales-Calderón et al. 2011; Cody et al. 2014). The termination of the *Kepler* prime mission due to a failure of a second reaction wheel and advent of the two-wheeled *K2* mission was a boon to YSO photometry since the latter observed several nearby star-forming regions: Taurus (1–3 Myr); ρ Ophiucus (~ 3 Myr); Upper Scorpius (~ 10 Myr). Only a minority of young stars observed by *K2* exhibit dipping, but this could be a completeness (duty cycle) effect since these stars have only been observed for 70–80 days.

As in the case of UX Orionis stars and AA Tau, dips are thought to be produced by dust, but the mechanism(s) and connection to the circumstellar disk and planet formation remain poorly understood. Besides AA Tau-like accretion flows (Bodman et al. 2017), instabilities such as the Rossby wave instability could produce vertical structures in the disk that periodically occult the central star (Stauffer et al. 2015; Ansdell et al. 2016b). Disk-based scenarios predict that the disks of dipper stars should be highly inclined to the line of sight. The outer regions, at least, of disks can be resolved by the Atacama Large Millimeter Array (ALMA) but the vast majority of these are *not* highly inclined (Ansdell et al. 2016a). Appeals to a warped inner disk may be applicable in some cases (Loomis et al. 2017; Mayama et al. 2018), but the limited work inside 1 AU on the brightest handful of objects with infrared interferometers shows moderately inclined in-

ner disks as well. (Vural et al. 2014; Davies et al. 2018a,b). Alternative explanations for dips include dust lofted in disk winds, for which there is indirect support in other systems (Varga et al. 2017; Fernandes et al. 2018; Ellerbroek et al. 2014), gravitationally bound clumps of planetesimals (Ansdell et al. 2016b), or disintegrating comet-like planetesimals (Kennedy et al. 2017).

Transient dimming is rare but nevertheless does occur among main sequence stars that lack substantial disks. These instances are important clues for understanding the full potential range of different circumstellar reservoirs and sources of dust. Low-amplitude ($\lesssim 1\%$) quasi-periodic dipping with Keplerian regularity but varying amplitude and shape has been explained by dust clouds emanating from “evaporating” ultra-short period planets which by themselves are too small to produce a detectable transit signal (Rappaport et al. 2012; Sanchis-Ojeda et al. 2015). Low-amplitude dips with shapes consistent with transiting “exocomets” have been identified in the light curves of several main sequence stars, none of which have detectable infrared excess indicative of disks (Rappaport et al. 2018; Ansdell et al. 2019; Zieba et al. 2019); the transiting objects could be larger analogs to the Sun-grazing comets discovered by the SOHO satellite (Battams & Knight 2017; Jones et al. 2018). The anomalous star KIC 8462852 (Boyajian et al. 2016) may be the extreme member of a population of such stars (Wyatt et al. 2018). Dips have also been detected in the light curve of at least one star that has evolved well beyond the main sequence, i.e., the white dwarf WD 1145+017 (Vanderburg et al. 2015). The transiting objects causing the dips are thought to be one or more evaporating, tidally disrupted planetesimals, a scenario consistent with observations infrared excess from circumstellar dust and accretion of heavy elements into the white dwarf atmosphere.

The transitional era between the YSO and mature stellar phases, populated by ~ 100 Myr-old stars near the zero-age main sequence, could also illuminate the dipper phenomenon. An example is RZ Piscium, an isolated, post-T Tauri star that is pre-main sequence but older than most dipper stars (30–50 Myr Grinin et al. 2010; Punzi et al. 2018), has both UX Ori-like dimming and a substantial infrared excess from circumstellar dust (de Wit et al. 2013). Its identification as a UX Ori-like variable was serendipitous since it lies well above the Galactic plane, far from any known star-forming region or known cluster, and lacks the defining attributes of a YSO.

The *Gaia* all-sky astrometric survey will revolutionize our knowledge of young stars in the Solar neighborhood (Lindgren et al. 2018), in particular by identifying new members in young (co-) moving groups (YMGs) that are more kinematically than spatially clustered (Faherty et al. 2018; Tang et al. 2019). The *Transiting Exoplanet Survey Satellite* (*TESS*) is obtaining precise photometry of stars over 85% of the sky with a cadence of ≤ 30 min for at least 27 days (Ricker et al. 2014), permitting identification of dipper stars in these dispersed groups and even refining ages of the groups by gyrochronology (Curtis et al. 2019). This *Gaia*-*TESS* synergy can be the basis of a broad, sensitive search for dipper stars with ages of tens to hundreds of Myr.

Here we report that a *TESS* light curve of HD 240779, the primary component of a visual ($\rho = 5''$) binary, reveals it to be a dipper star (Fig. 1), and that other ground- and

space-based observations suggest that it is a member of the ≈ 125 Myr-old AB Doradus Moving group (ABDMG). In Section 2 we present the data from *TESS* and other observations; in Section 3 we validate the source of the dip signal, determine stellar and orbital parameters, analyze the infrared excess due to circumstellar dust, and assess the age and moving group membership of the binary. In Section 4 we summarize our findings and discuss the origin of the material responsible for the dipping and infrared excess, and compare this intriguing system to its closest published counterparts.

2 OBSERVATIONS AND DATA REDUCTION

2.1 *TESS*

The binary consists of HD 240779 and BD+10 714B and was confirmed in *Gaia* Data Release 2 (Lindgren et al. 2018) to be a physical pair at a distance of 95.2 ± 0.4 pc (Table 1). The stars appear as sources 284730577 and 284730578 in the *TESS* Input Catalog (TIC) with *TESS* magnitudes $T = 9.16$ and $T = 9.98$ (Stassun et al. 2018). The stars were observed by *TESS* during Sector 5 (orbits 17 and 18) from 15 November to 11 December 2018 in CCD detector 3 of Camera 1. Cutouts (11 pixel \times 11 pixel or $132'' \times 132''$) of the photometer images containing the two unresolved sources as well as source-free pixels for background subtraction were retained at 2-sec intervals and combined by onboard processes into a 2-min cadence sequence of images with a clipping algorithm to remove charged particle events prior to transmission to ground stations. Figure 2 is a mean image constructed from the entire sequence. Besides the stars of interest, the only other stars of consequence (*TESS* magnitude $T < 15$, or at least 1% as bright as the target stars) are plotted as white points in the figure. Of particular interest is TIC 284730592 ($T \approx 12.0$), which may contribute a small amount of flux to the extracted light curve of TIC 284730578 and perhaps TIC 284730577, but cannot be the source of the dipping (see Section 3.1). A 18944-point light curve for each star was generated by the Science Processing Operations Center (SPOC; Jenkins et al. 2016) using an optimized aperture centered on the position of each source, and subtracting a background signal from another aperture that avoids all sources in the cutout. The light curves of the two stars are essentially identical since the aperture is more than an arc-minute across and includes both stars. The light curve of the primary is shown in Fig. 1.

TESS light curves are manually inspected by a team of citizen and academic scientists for notable phenomena, including dips. The search is conducted using *LcTools*¹, a free and publicly available software program that provides a set of applications for efficiently building and visually inspecting large numbers of light curves (Kipping et al. 2015). For more details on the *LcTools* package and the visual survey methodology, see Rappaport et al. (2018). TIC 284730577/8 was identified as a light curve of interest on 3 March 2019. The light curve and image data were retrieved from the Mikulski Archive for Space Telescopes (MAST).

2.2 Keck-1/HIRES

We observed HD 240779 and BD+10 714B with the HIRES spectrometer (Vogt et al. 1994) at the W. M. Keck Observatory on UT 26 March 2019. We used an exposure meter to stop the exposures after achieving a signal-to-noise ratio of 40 per pixel at the peak of the blaze function in the spectral order containing 550 nm light. The spectral format and HIRES settings and reduction were identical to those used by the California Planet Search (CPS; Howard et al. 2010). We used the C2 ($14'' \times 0.86''$) entrance aperture of the decker mechanism and performed sky subtraction to reduce contamination from scattered light in the spectrograph. The spectral coverage is from 3640 to 7990 Å.

3 ANALYSIS

3.1 Validation, Characterization and Source of Transient Dimming

Transient dimming events or “dips” in the 2-min light curve of TIC 247306577/8 were identified by eye and highlighted in grey in Fig. 1. These do not correspond to times of the momentum dumps (vertical dotted red lines) indicating that they are unrelated. *TESS* detector pixels subtend $21''$, meaning that confusion and mis-identification of a signal in an extracted light curve, particularly very faint signals typical for planetary transits, are possible. In the case of the dips, the source cannot be fainter than $\approx 10\%$ (2.5 magnitudes) of the binary system. The only nearby source that satisfies this requirement is TIC 2843730592 ($T \approx 12.0$), but this source is 1 arc-minute away and outside the aperture, so its flux contribution must be $\ll 10\%$. A difference image constructed by subtracting the mean of images during dips from the mean of images in equal intervals before and after each dip (Fig. 3) shows that the “missing” flux during dips is centered on the location of the system, demonstrating that this *is* the source of the dimming signal. The centroid location of the difference signal, marked by the black dot in Fig. 3, is only 0.2 pixels or $4''$ to the N of the mean source centroid (Fig. 2), a distance much smaller than the angular resolution of *TESS* and comparable to the binary separation. Another potential source of false positives for dips is contamination of the background aperture by a variable or moving source, e.g., an asteroid. We constructed a video using the cutouts which revealed no moving or transient sources. Other distant sources can be the source of faint signals, e.g. by “sticking” of charge from a bright variable star like an eclipsing binary (Gaidos et al. 2017) but these effects are unlikely to produce a 10% signal in a bright star.

We conclude that the binary system HD 240779+BD+10 714B is responsible for the signal, but which star of the two (or both?) is involved? The components of this system are obviously not resolved by *TESS*. However, the position of the unresolved source detected by *TESS* should lie at a flux-weighted position along a line between the two stars, and changes in the brightness of either star should induce a shift in the centroid $\gtrsim 0.01$ pixels which might be detected. The magnitude and sign of the centroid shift depend on which star is dimming. We projected the relative position of the moment-weighted centroid as supplied in the light curve file

¹ <https://sites.google.com/a/lctools.net/lctools>

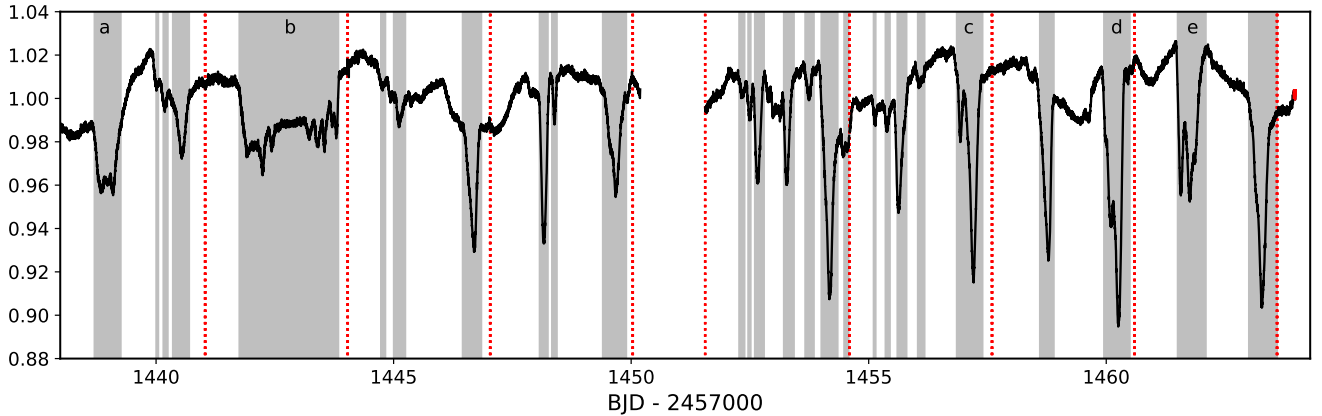


Figure 1. Normalized Sector 5 light curve from *TESS* 2-minute cadence data for an aperture centered on TIC 284730577/8. Red points have quality flags set. Vertical dashed red lines mark times where the spacecraft’s hydrazine thrusters remove spin from the momentum wheels. The interruption between 1450 and 1452 days is due to the spacecraft halting observations to transmit data at orbital perigee. Grey regions are manually-selected dimming events or “dips”.

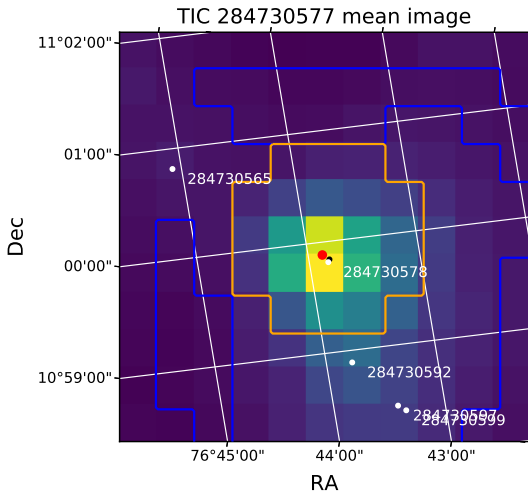


Figure 2. Mean *TESS* photometer image from Sector 5 observations of TIC 284730577 and 284730578. The red point marks 284730577; other stars brighter than *TESS* magnitude $T = 15$ are marked by white points. The black point is the flux centroid within the aperture. Source and background apertures used to construct the light curve (Fig. 1) are outlined by orange and blue lines, respectively.

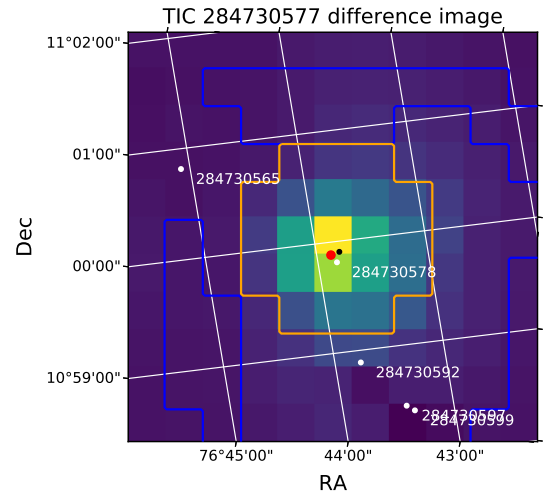


Figure 3. Difference image constructed by subtracting the mean of images during dips (demarcated by the grey regions in Fig. 1) from the mean of images in an interval of equal duration before and after each of the dips. The black dot marks the centroid location of the difference signal. Its near coincidence with the mean source centroid (Fig. 2) demonstrates that the dipping signal is co-located with the binary star system.

header (MOM_CENT1 and MOM_CENT2) onto the bisector using the map projection coefficients supplied in the file. The centroid drifts by several tenths of a pixel over the course of Sector 5 and this trend was removed with a $N = 301$ running median filter. Figure 4 shows the residual centroid shifts vs. the normalized flux. Red points are those within the dips indicated by the grey zones in Fig. 1; grey points are all others. The grey line is running median of the points within dips and the black points are the robust means in 101-point bins. A comparison with the expected motion

(dotted magenta and dash-dotted blue lines) supports the primary star as the source of the dipping signal.

Dimming events as deep as 10% are superposed on irregular variability of about $\pm 2\%$. While most of these dips are much shorter than a day and have distinct minima, several (marked c, d, and e in Fig. 1) appear to be double events, and two (marked a and b) are either single, long (1-2 day) events or composites of many unresolved events. A Lomb-Scargle periodogram (Scargle 1982) of the entire light curve (solid line in Fig. 5), contains peaks at 1.51 and 4.2 days. In a periodogram of the light curve after excision of the

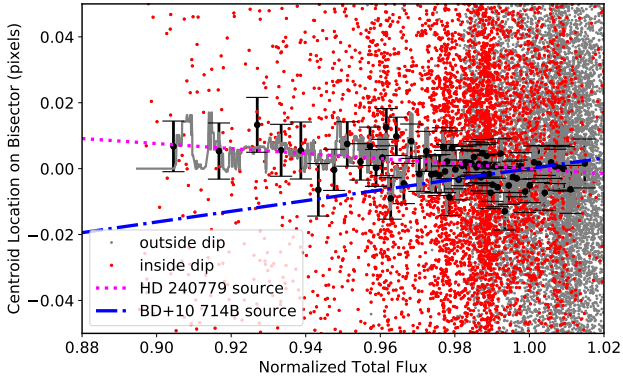


Figure 4. Relative position of the centroid of the unresolved *TESS* source containing flux from both HD 240779 and BD+10714B, projected along the bisector between the two stars (positive towards BD+10714B) vs normalized flux. The grey line is a running median filter with $N=101$, the black points are robust (3σ clipping) means in bins of 101 points, with errors determined by 100 bootstrap with resampling. The dotted magenta and dash-dot blue lines are the predicted trends based on a flux ratio in the *TESS* bandpass of 2.13. Centroid motion is consistent with HD 240779 as the source of the dips.

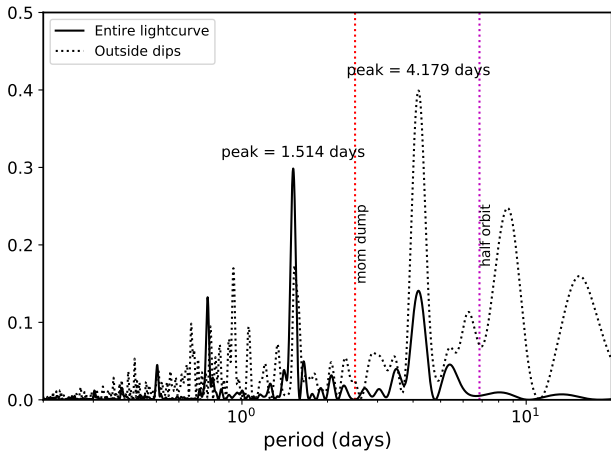


Figure 5. Lomb-Scargle periodogram of the *TESS* light curve, showing the peak at 1.51 days corresponding to dips. The signal at ≈ 4.2 days could be due to rotational variability. These signals are clearly distinct from any artifacts produced by removal of momentum from the reaction wheels and motion of the spacecraft during an orbit (vertical dotted lines). The dotted curve is the periodogram constructed after removal of dipping intervals (grey bands in Fig. 1). The signal at ≈ 0.8 days in the excised light curve could be a harmonic or alias of 1.51 days.

manually-identified dips, the 1.51 day-signal is suppressed and the 4.2 day signal is enhanced (dotted line in Fig. 5). This indicates that the dipping is responsible for the 1.5-day signal. Phased to this period (Fig. 6, the signal reveals its quasi-periodic nature, ruling out an eclipsing binary as the source. We identify the 4.2-day with the rotational signal of the star (see Sec. 3.5).

We quantified the overall morphology of the light curve

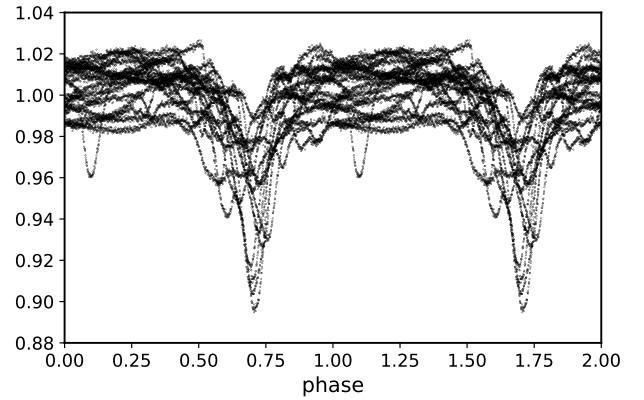


Figure 6. Normalized *TESS* light curve phased to 1.51 day period and repeated, showing the quasi-periodic nature of the signal.

to compare it with other dippers and variable stars using the asymmetry of the distribution of values, and the extent to which the lightcurve is quasi-periodic or aperiodic, that is to say the variability cannot be described by a single periodic signal. To describe these properties, the asymmetry M and quasi-periodicity Q parameters defined by Cody et al. (2014) were calculated. $M \in [-\infty, \infty]$ and a light curve with $M = 0$ has a symmetric amplitude distribution, while one with $M = +1$ or $M = -1$ has many more negative- or positive- going points, respectively. $Q \in [0, 1]$; a light curve with $Q = 0$ is perfectly periodic while having $Q = 1$ is stochastic (no periodicity), and light curves with intermediate values of Q are quasi-periodic, i.e. the periodic signal changes shape or amplitude, and/or there is additional variability at other timescales. Dippers have $M > 0$ while “bursters” (stars with flaring and/or episodic accretion have $M < 0$). Rotational variables tend to have $M \approx 0$ and small Q . The lightcurve of HD 240779 + BD+10714B has $M = 0.82$ and $Q = 0.45$, placing it within the regime of quasi-periodic dippers in a Q - M space (Fig. 7). The overall variability amplitude (2%) is modest compared to those of known dippers.

3.2 Stellar Parameters

HIRES spectra were extracted and processed using the procedures described in Howard et al. (2010). Spectra were matched to [synthetic/observational] library spectra using *SpecMatch Synthetic* and *SpecMatch Empirical* (Petigura 2015; Petigura et al. 2017; Yee et al. 2017). The derived parameters are reported in Table 1. In addition, barycentric radial velocities (RVs) were derived and a search for additional sets of lines ruled out confused (spectroscopic binary) companions to a contrast ratio of 1%. Parameters were also estimated with the T_{eff} and $[\text{Fe}/\text{H}]$ from the HIRES spectrum and an absolute K_s -band magnitude using *ISOCLASSIFY* (Huber et al. 2017). These tools contain no special provisions for accurately determining ages or fitting young stars; *SpecMatch Empirical* uses a spectral library of middle-aged stars and there is no age prior for *ISOCLASSIFY*.

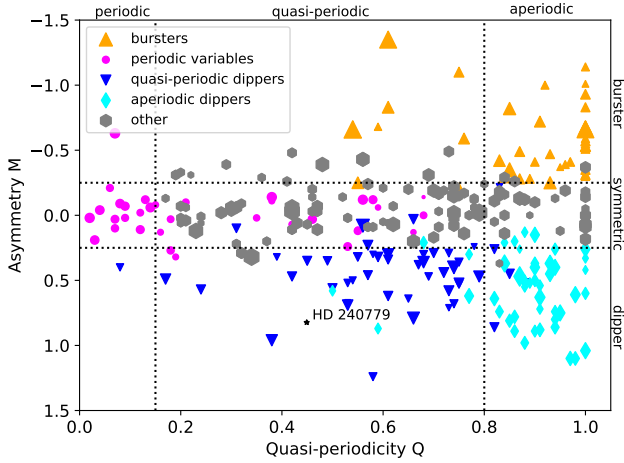


Figure 7. Asymmetry Q and quasi-periodicity M parameters of the *TESS* light curve of HD 240779 (black star) compared to *K2* light curves of variable stars in the Upper Scorpius and ρ Ophiucis star-forming regions as determined by Cody & Hillenbrand (2018), using the definitions of Q and M defined in Cody et al. (2014). Marker sizes are colored according to the visual classification of Cody & Hillenbrand (2018) and scaled by the square root of the variability amplitude. The marker for HD 240779 is also scaled to show its comparatively low variability. The dotted lines mark the notional boundaries between the classes suggested by Cody & Hillenbrand (2018).

3.3 Orbit Fitting

Gaia parallaxes and proper motions of the two components indubitably show them to be at the same distance (within errors) and nearly the same sky-projected motion. With a projected separation of ≈ 500 AU and hence orbital period of many thousands of years, obtaining a true astrometric orbit is not possible. However, a family of possible orbits can be identified and the range of possible orbital parameters constrained using current positions and motions. Acceptable orbits were identified using the LOFTI implementation of the Orbits For the Impatient code (OFTI) (Blunt et al. 2017; Pearce et al. 2019), using the constraints of the current *Gaia* separation and proper motions of each component, the RVs at a single epoch ≈ 3.5 yr after *Gaia* DR2 (2015.5) (Table 1) and an inferred total system mass (the empirical values from Table 1). An initial semi-major axis “guess” of 220 AU and a uniform prior for eccentricity were used. Figure 8 plots 100 randomly-selected sky-projected orbits from the sample, colored by phase relative to the current epoch. Figure 9 plots the periastron distribution of 25535 accepted orbits as an indicator of the maximum potential gravitational interaction between the stars. The distribution is very broad, with peaks near 90 AU and 600 AU. The possibility that the periastron is < 100 AU has implications for the structure of the disk around HD 240779 and the mechanism responsible for the transient dimming (Sec. 4).

3.4 Infrared Excess

The system is resolved by the 2MASS survey and the source positions (adjusted to epoch 2015.5 using *Gaia* DR2 proper

Table 1. Stellar parameters

Parameter	SpecMatch (Empirical)	SpecMatch (Synthetic)	Isoclassify plus <i>Gaia</i>
HD 240779 (TIC 284730577)			
T_{eff} [K]	5791 (110)	5793 (100)	5780 (103)
R_* [R_{\odot}]	0.96 (0.10)	0.97 (0.06)	1.03 (0.01)
Fe/H	+0.04 (0.09)	+0.07 (0.06)	+0.03 (0.09)
log g	—	4.58 (0.10)	4.41 (0.03)
M_* [M_{\odot}]	—	1.01 (0.04)	1.00 (0.05)
log age [yr]	—	9.36 (0.42)	9.63 (0.26)
RV [km s $^{-1}$]	+14.86 (0.10)		
$v \sin i$ [km s $^{-1}$]		11.0 (1.0)	
d [pc]		94.7 (0.5)	
BD+10 714B (TIC 284730578)			
T_{eff}	5099 (110)	5193 (100)	5070 (80)
R_* [R_{\odot}]	0.78 (0.10)	0.83 (0.04)	0.79 (0.01)
Fe/H	+0.04 (0.09)	+0.15 (0.06)	0.03 (0.08)
log g	—	4.66 (0.10)	4.55 (0.03)
M_* [M_{\odot}]	—	0.88 (0.03)	0.83 (0.03)
log age [yr]	—	9.62 (0.42)	9.75 (0.3)
RV [km s $^{-1}$]	+16.04 (0.10)		
$v \sin i$ [km s $^{-1}$]		6.2 (1.0)	
d [pc]		95.6 (0.6)	

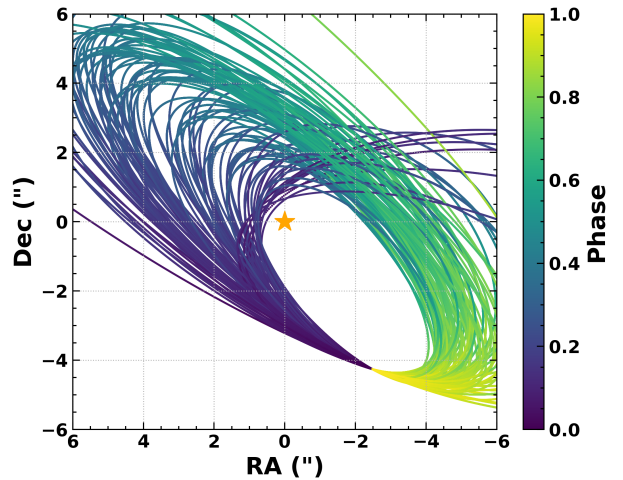


Figure 8. Subset of possible orbits of BD+10 714B relative to HD 240779 (marked as the star) constrained by *Gaia* astrometry, an RV measurement for each star, and spectroscopically-based mass estimates.

motions) correspond within errors to the *Gaia* DR2 positions of the stars (Fig. 10). Images in the individual *WISE* 1–4 passbands were downloaded from the NASA/IPAC Infrared Science Archive and the source associated with this system inspected. In no bandpass was the binary resolved, although in the highest resolution image (W1, 6.1”) the source is elongated in the NE–SW direction of the binary. The centroid of each source were determined by fitting elliptical Gaussians as implemented by DAOSTARFINDER in the PHOTUTILS package in Python. These are plotted in Fig. 10

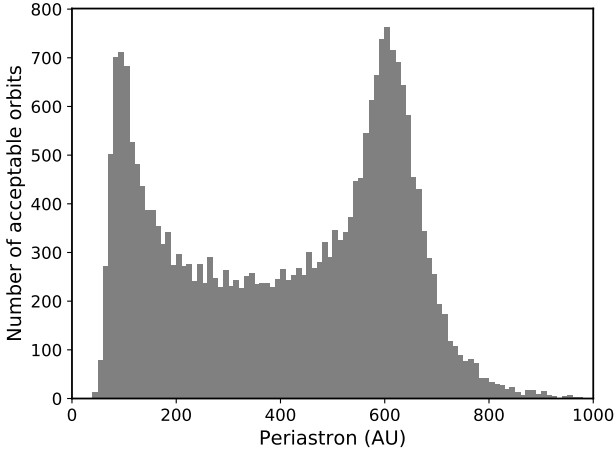


Figure 9. Distribution of possible periastra of 25535 orbits of HD 240779 + BD+10 714B that satisfy constraints imposed by *Gaia* and an RV measurement.

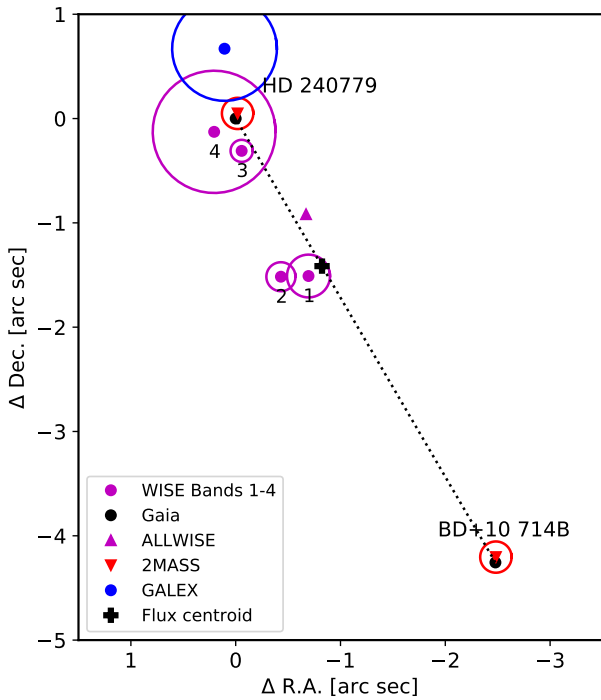


Figure 10. Epoch 2015.5 relative positions of HD 240779 and BD+10 714B as measured by *Gaia* along with infrared sources from 2MASS (red) and WISE (magenta). Infrared source locations have been adjusted to 2015.5 using *Gaia* proper motions. The circles are scaled to the errors in position.

along with the ALLWISE source position. While the ALLWISE (Cutri et al. 2013) and W1 and W2 positions correspond to the expected flux centroid calculated from K_s magnitudes, the W3 ($12\mu\text{m}$) and W4 ($22\mu\text{m}$) sources fall on the position of the HD 240779, indicating that it is the source of the detected infrared excess.

Figure 11 plots flux density vs. effective wavelength for

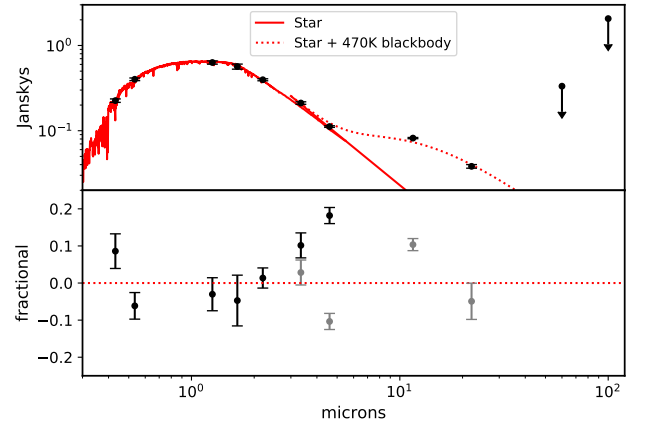


Figure 11. Top: Spectral energy distribution of HD 240779 using *Tycho*, 2MASS, and *WISE* photometry. The solid red line is a PHOENIX model atmosphere with parameters ($T_{\text{eff}}=5800\text{K}$, $\log g = 4.5$, $[\text{Fe}/\text{H}] = 0$, $[\alpha/\text{Fe}] = 0$). The dashed red line includes a 470K blackbody, i.e. due to circumstellar dust. Bottom: difference between the SED and stellar atmosphere model (black points) and star + blackbody (grey points).

HD 240779 based on resolved photometry from *Tycho* (B_T and V_T), 2MASS (JHK_S), and *WISE* (channels W1-4 with effective wavelengths of 3.4, 4.6, 12, and $22\mu\text{m}$). W1 and W2 flux densities were proportioned between HD 240779 and BD+10 714B according to their relative brightness in K_s -band. The system is unresolved in AAVSO Photometric All Sky Survey (APASS) and was not observed by *Spitzer*, *Herschel*, or at (sub)mm wavelengths. Effective wavelengths and zero points were drawn from Mann & von Braun (2015). A smoothed model PHOENIX spectrum from (Husser et al. 2013) with $T_{\text{eff}}=5800\text{K}$, $[\text{Fe}/\text{H}]=0$, $\alpha/\text{Fe}=0$, $\log g = 4.5$ with a best-fit normalization, plus a λ^{-4} Rayleigh-Jeans extension, is shown. The fit is markedly improved ($\chi^2 = 7.5$ $\nu = 3$ degrees of freedom) by the inclusion of reddening ($E_{B-V} = 0.11$). Extinction maps (e.g., Green et al. 2018) are not properly calibrated within ~ 100 pc, but negligible reddening is expected with the “Local Bubble” ($d \ll 100$ pc). However, we caution against interpreting this as evidence for circumstellar reddening, since the star is variable in the optical and the *Tycho* and 2MASS observations were at different epochs.

Excess emission is obvious in the *WISE* W3 ($12\mu\text{m}$) and W4 ($22\mu\text{m}$) channels, but less evident in the W1 ($3.4\mu\text{m}$) and W2 ($4.6\mu\text{m}$) channels. This is consistent with the W1 and W2 photocenters coinciding with the K_s -band centroid (presumably dominated by photosphere flux) between the two stars (Fig. 10). The excess is approximately consistent with a 470K blackbody with a solid angle of 2.8×10^{-17} Sr or about 170 times that of the stellar photosphere. A blackbody model added to the Rayleigh-Jeans extension of the stellar model is plotted as a dotted red line in the top panel of Fig. 11 and the difference between the observations and model plotted as the grey points in the bottom panel. Unsurprisingly, the data are not well fit by a single-temperature blackbody, which may mean a range of dust temperatures or silicate emission near $10\mu\text{m}$. The inferred fractional luminosity, assuming a blackbody spectrum, is $L_{\text{dust}}/L_* = 2 \times 10^{-3}$.

3.5 Young Moving Group Membership and Age

Unlike nearly all previously identified dipper stars, the HD 240779 + BD+10714B system is not a known or proposed member of a nearby star-forming region. However, precise parallaxes and proper motions from *Gaia* plus the HIRES radial velocity were used to calculate Galactic *UVW* space motion and show a kinematic link with the ≈ 125 Myr-old Pleiades cluster and AB Doradus moving group (ABDMG, Fig. 12. Color-magnitude diagrams (Luhman et al. 2005; Barenfeld et al. 2013) and a “traceback” age of 125 Myr (McCarthy & Wilhelm 2014) suggest a kinematic and chronological connection to the Pleiades (Ortega et al. 2007).

The Bayesian **Banyan Σ** algorithm, which uses both *UVW* and space coordinates *XYZ* (Gagné et al. 2018), indicates a 44% probability of membership in the ABDMG and negligible probability for every other cluster and moving group in the database, including the Pleiades; the remainder probability is assigned to the field. This system lies 60 pc from the center of the Pleiades, well outside the 13 pc tidal radius of the cluster (Adams et al. 2001). Likewise, this system is more distant than typical ABDMG members, although the dispersion of that group is larger and more poorly known.

Lithium abundance is a widely-used chronometer for solar-type stars. Because Li is destroyed as it is carried deep into the stellar interior by the surface convection zones of main sequence stars, the abundance of the element is observed to decrease with time, and more rapidly with cooler stars with deeper convection zones. We measured the equivalent width (EW) of the 6708 Å doublet of Li I following a procedure similar to that described in Berger et al. (2018). However, instead of using a Levenberg-Marquardt fit to measure the lithium equivalent width (EW), we utilized ROBOSPECT (Waters & Hollek 2013) which provided a better fit to the Li features while also ignoring the contribution of the blended Fe I line at 6707.441 Å. From the spectrum of HD 240779, we measured an $\text{EW}_{\text{Li}} = 143 \pm 6$ mÅ and 205 ± 7 mÅ for BD+10714B. Figure 13 compares these values with those of members of nearby young moving groups compiled from the literature. Measurements for the Pleiades are from measurements and compilation by Bouvier et al. (2018), for Ursa Majoris from Ammler-von Eiff & Guenther (2009), and all the remaining are from Mentuch et al. (2008). The abundance of Li in the HD 240779 + BD+10714B system falls well within the range spanned by the Pleiades and ABDMG, but not younger or older groups (Fig. 13).

Another widely used chronometer for solar-type stars is rotation. If a star is sufficiently spotted, rotation of the photosphere produces a sinusoidal-like signal in a light curve which can be identified by a periodogram or autocorrelation function.

Although an autocorrelation analysis (not shown) does not confirm the 4.2-day signal, it is consistent with the 4.4-day upper limit imposed by the $v \sin i$ and R_* of HD 240779 (Tab. 1), which is assumed to dominate the signal. Those of BD+10714B suggest a rotation period no longer than 6.6 days. Both these periods are consistent with a Pleiades-like age (Fig. 14).

The magnetic activity produced by a rotation-driven dynamo will heat the upper atmosphere of a star, produc-

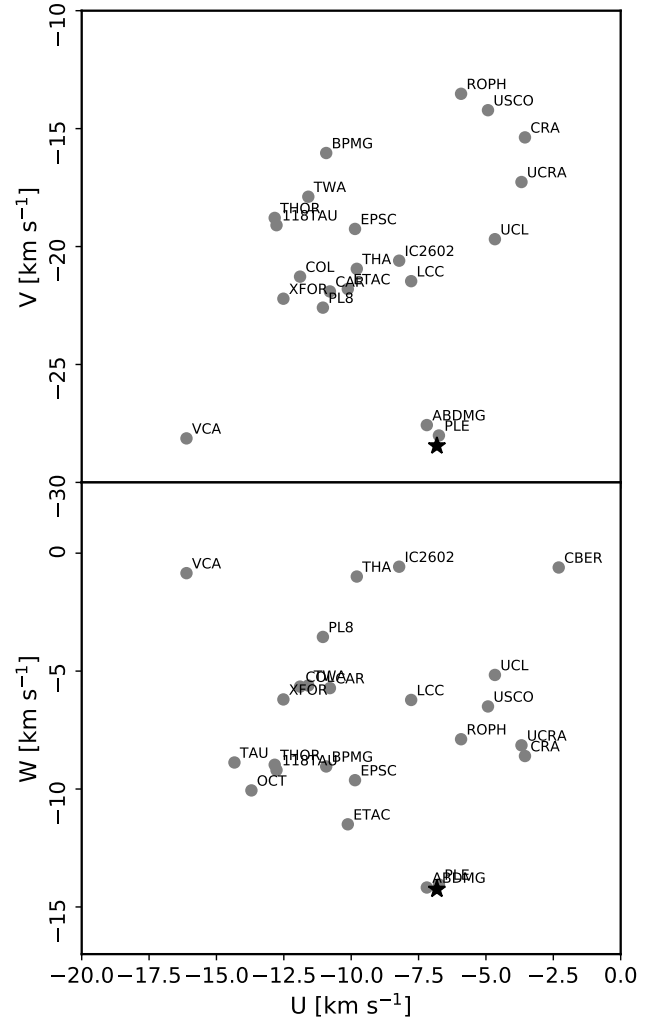


Figure 12. *UVW* Galactic space motion of the HD 240779 + BD+10714B system relative to the motions of clusters and moving groups of young stars in the **Banyan Σ** database (Gagné et al. 2018).

ing emission in the H and K lines of singly-ionized calcium, as well as many lines in the far and near ultraviolet wavelengths. The Ca II HK emission index R'_{HK} was calculated using the conversion constants for the Mount Wilson *S* index formula obtained in Wright et al. (2004), and the photosphere contribution (which must be subtracted) using the formula with $B-V$ color from Noyes et al. (1984). Values for $\log R'_{\text{HK}}$ of -4.40 and -3.95 were determined for HD 240779 and BD+10714B, respectively. In Fig. 15 these are compared to values from Pleiades stars from Mamajek & Hillenbrand (2008), with a conversion from $B-V$ color to T_{eff} from Pecaute & Mamajek (2013), and from Fang et al. (2018). The dipper system is far more magnetically active than the Sun (red bar in Fig. 15) and comparable in activity to Pleiades members.

The system was detected in both the near ultraviolet (NUV; 1770-2730 Å) and far ultraviolet (FUV; 1350-1780 Å) channels of the *Galax* space telescope (Bianchi et al. 2017).

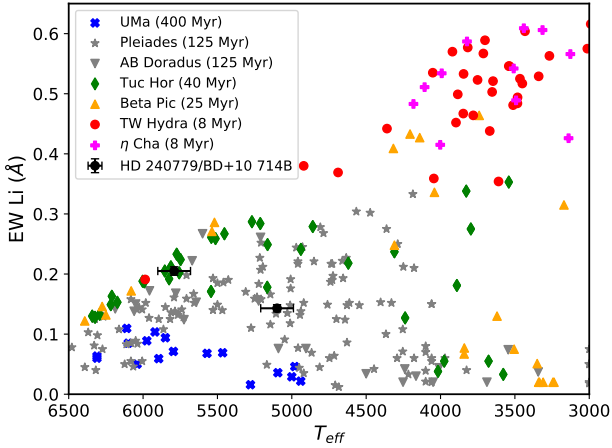


Figure 13. Li EW measured in spectra of HD 240779 and BD+10 714B, compared to those in nearby young moving groups, showing consistency with AB Dor and Ple age stars but not much younger or older groups.

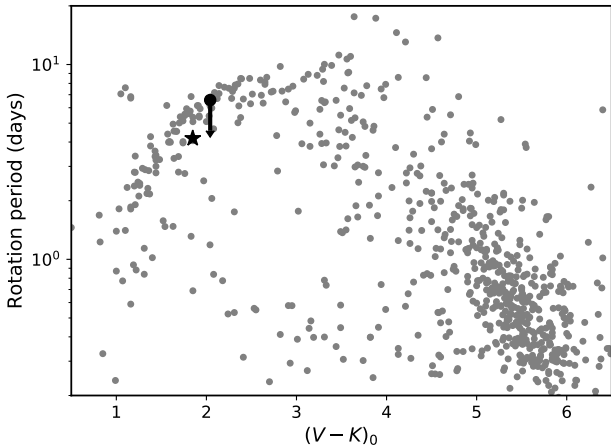


Figure 14. Possible rotation periods for HD 240779 (black star) and BD+10 714B (upper limit) compared to the distribution in 125 Myr Pleiades stars as measured from *K2* data by Rebull et al. (2016).

The NUV source coincides with the location of HD 240779 (Fig. 10 and the FUV-NUV source offset is 0."65, not significant compared to the positional uncertainty (0."47). The ratio of the flux density in the NUV over that in the K_s band is similar to that of known ABDMG members (Fig. 16) and the empirical relations of Findeisen et al. (2013) for young stars.

4 SUMMARY AND DISCUSSION

Like the photometric survey satellites that preceded it, *TESS* is expanding our knowledge of the scope of stellar variability, including that produced from occultation by circumstellar dust. *TESS* 2-min cadence observations of the

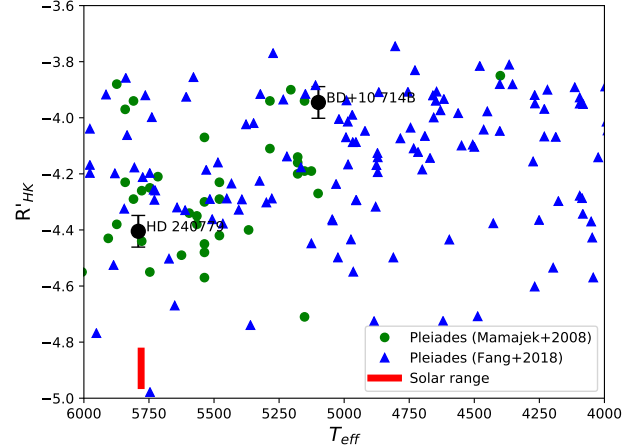


Figure 15. Chromospheric emission index R'_{HK} of compared to that of Pleiades stars from Mamajek & Hillenbrand (2008) and Fang et al. (2018). The red bar is the range spanned by the quiet and active Sun.

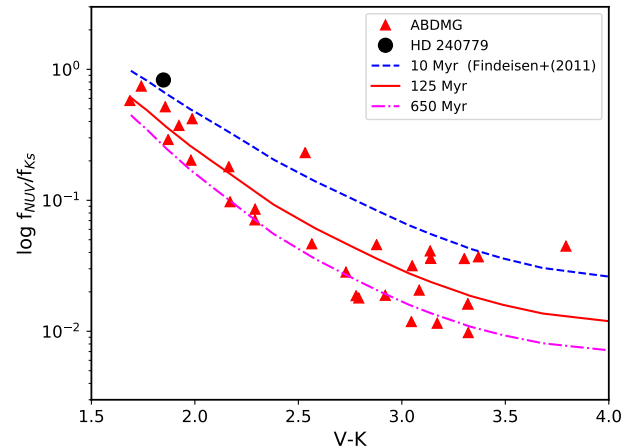


Figure 16. NUV to K_s -band flux density of HD 240779 vs $V-K_s$ color compared to empirical relations from Findeisen et al. (2013) for three stellar ages (curves) and to confirmed AB Doradus Moving Group members (red triangles, J. Gagné, personal communication).

solar-type primary HD 240779 of a double star yielded a 27-day light curve containing multiple dimming events, each lasting a fraction of a day with attenuation up to 10%, and often spaced by 1.5 days. The asymmetry and quasi-periodicity of the light curve, as quantified by the M and Q parameters of Cody et al. (2014), distinguish it from those of rotational variables and classify it as a quasi-periodic dipper, although some anomalous young, very fast-rotating M dwarfs also have light curves that are highly periodic but asymmetric in time and amplitude for reasons that are not understood (Stauffer et al. 2018; Zhan et al. 2019).

The binary system's barycentric space motion matches closely with that of the 125 Myr Pleiades and the AB Doradus Young Moving Group, but its position clearly rules

out membership in the Pleiades. Measurements of Li abundances, Ca II HK line emission, and NUV emission are all consistent with a 125 Myr age and thus this system could belong to a spatially extended ABDMG, or a larger, kinematically connected population that is coeval with the Pleiades and ABDMG. The metallicity of HD 240779 and BD+10 714B found by analysis of a high-resolution spectrum (Table 1) are slightly but not significantly (0.1 ± 0.1) above that of the AB Doradus moving group (McCarthy & Wilhelm 2014). But if this system is as young as 125 Myr, i.e. zero-age main sequence, then obviously the isochrone-based ages reported in Table 1 are incorrect and some other parameters are systematically in error, since they are determined self-consistently with those ages. While T_{eff} and R_* may be robust, M_* and thus $\log g$ will be underestimated, and due to covariance between $[\text{Fe}/\text{H}]$ and $\log g$ (Torres et al. 2006), metallicity is overestimated.

HD 240779 is significantly older than most other dippers, which are typically found in $\lesssim 10$ Myr-old star-forming regions, as well as the 30-50 Myr-old UX Ori-type variable RZ Piscium (Punzi et al. 2018). It joins a small number of known main sequence systems and evolved stars that exhibit transient dimming, e.g. R Corona Borealis stars (Montiel et al. 2018), a white dwarf with disintegrating planetesimals (Vanderburg et al. 2015), stars with “exocomets” (Rappaport et al. 2018; Ansdell et al. 2019), and the enigmatic F dwarf KIC 8462852 (Boyajian et al. 2016). HD 240779 also falls in a region of the Rosenberg-Hertzsprung-Russell diagram between the higher-mass Herbig Ae/Be UX Orionis stars and the lower-mass M-type dippers where young stars with transient dimming are uncommon, or at least rarely found.

HD 240779, but not its K-type companion, has emission significantly in excess of the photosphere in the *WISE* 12 and 22 μm channels indicative of circumstellar dust. In contrast to most young dipper stars, e.g., those observed by *K2* in the 3-10 Myr-old ρ Ophiuchus and Upper Scorpius star-forming regions (Ansdell et al. 2016b; Cody & Hillenbrand 2018), there is little or no excess emission at 3.4 and 4.6 μm (Fig. 17), nor is there any emission in $H\alpha$ or the forbidden lines of oxygen indicative of accretion. This indicates the absence of an inner disk, although this deficiency does not conflict with the amount of dust that is required to produce the dips alone, even if that dust is hot. Assuming emission at the maximum (dust sublimation) temperature of 1500K, the radiation of the dust that produces a 10% dip would be 0.7% and 1% of the photosphere at 3.4 and 4.6 μm , respectively, and would be obscured by measurement error (Fig. 11).

The excess emission at longer wavelengths resembles that of a blackbody at 470K and the inferred fractional infrared luminosity is $L_{\text{dust}}/L_* \approx 2 \times 10^{-3}$, within the range of “debris disks” (Hughes et al. 2018). The only dipper star in the Cody & Hillenbrand (2018) sample that lacks significant excess emission at 3.4 and 4.6 μm is EPIC 205238942, an M0-type member of Upper Sco (confirmed by *Gaia* DR2 astrometry) with a strong rotational signal (period = 9.3 days) and stochastic dips of up to $\sim 15\%$. In these respects the stars are more “evolved” relatives of RZ Piscium, a UX Ori-like star with much deeper dips (up to 2.5 magnitudes) and a much larger infrared excess ($L_{\text{dust}}/L_* \approx 0.08$) that is

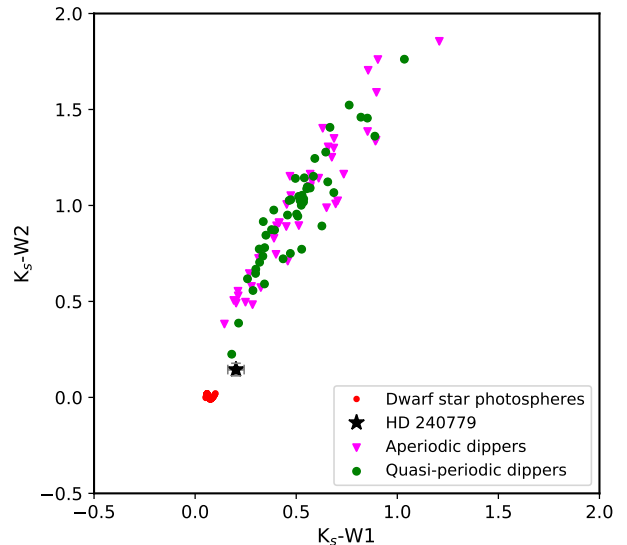


Figure 17. Excess infrared emission in the *WISE* W1 (3.4 μm) and W2 (4.6 μm) channels relative to 2MASS K_s (2.2 μm), for HD 240779 (shown as star symbol with error bars) relative to stars with aperiodic and quasi-periodic dipping identified by Cody & Hillenbrand (2018) in Upper Scorpius and ρ Ophiuchus star-forming regions. Also shown are the colors of photospheres of 3800-8300K dwarf stars from Jian et al. (2017).

adequately described by dust at a single (500K) temperature.

In this case, the lack of a substantial inner disk eliminates some of the proposed mechanisms involving accretion (Bouvier et al. 2013) or vertical structures in a disk (Ansdell et al. 2016b). Impact disruption of asteroidal bodies or giant impacts during the final phase of rocky planet formation (Morbidelli & Raymond 2016) have been invoked to explain warm dust around 30-50 Myr-old RZ Piscium, the 25 Myr-old β Pictoris Moving Group member HD 172555 (Johnson et al. 2012), and ID8, a star with a rapidly time-varying excess in the ~ 35 Myr cluster NGC 2547 (Su et al. 2019). Something analogous to these impact-driven disks might explain the excess infrared emission of 125 Myr-old HD 240779. The dust required to produce the dips of HD 240779 is equivalent to a 100-km size body that has been completely disrupted into 10 μm grains, and 470K corresponds to the temperature expected of dark grains on the orbit of Mercury. The lifetime of dust against Poynting Robertson drag at this distance is $\sim 10^3$ yr, and thus the dust is ephemeral. Warm, 12 μm excess-producing dust is rare ($\sim 1\%$) around young (< 120 Myr), non-T Tauri-like stars (Kennedy & Wyatt 2013), which might explain why HD 240779 has detectable dust but BD+10 714B does not.

This leaves the question of the nature and origin of the material responsible for the quasi-periodic signal at 1.51 days. The phased signal (Fig. 6 more closely resembles the periodic dippers found in Upper Sco (Ansdell et al. 2016b) and is more ephemeral and irregular than that of the “evaporating” planets Kepler-1520b and K2-22b (Rappaport et al. 2012; Sanchis-Ojeda et al. 2015), suggesting a different mechanism. If the period is that of a Keplerian orbit,

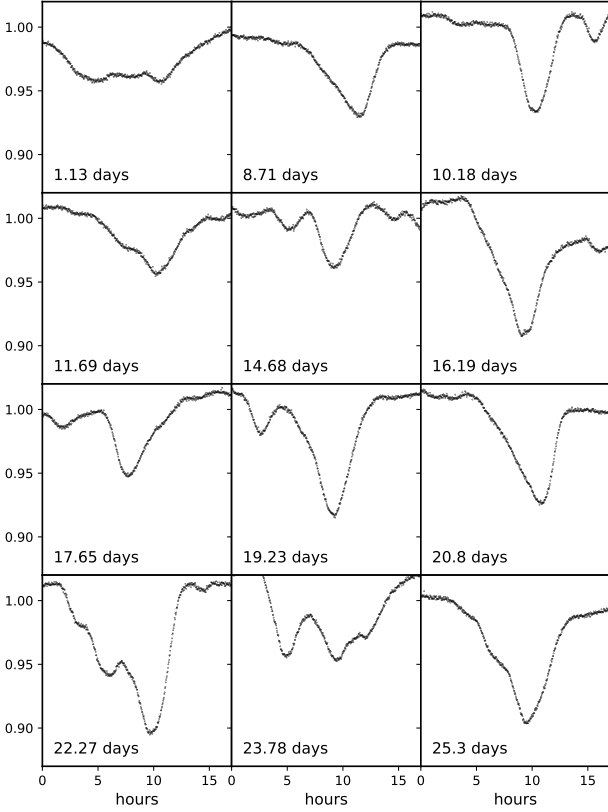


Figure 18. Gallery of the 12 deepest dips, in order of occurrence.

the semi-major axis is about 6 stellar radii, If we have correctly identified the stellar rotation period (4.2 days) then this material is orbiting within the stellar co-rotation radius. The maximum transit duration of obscuring objects much smaller than the star and on a circular 1.51-day orbit is 2 hrs, thus a light curve should *not* contain structure on much shorter timescales. Fig. 18 illustrates the smoothness of the light curves of the largest dips at intervals less than a few hours, and Fig. 19 shows that the roll-off in periodogram power begins at around 5 hours and is complete at 2 hours. The lack of structure in the light curve at intervals between 2 and 5 hours could simply mean that occulting dust is distributed or clustered on scales comparable to the stellar disk as well as eccentric orbits. This is certainly suggested by the extended and composite dips in Figs. 1 and 18.

The obscuring dust could arise from planetesimals that are disrupting due to tides or stellar irradiation. For the Roche limit to extend to 6 stellar radii, the density of a strengthless (fluid) body would have to be $\leq 0.1 \text{ g cm}^{-3}$, well below that of rubble-pile asteroids or comets (Carry 2012). The equilibrium temperature of dark surfaces at this separation is $\approx 1700\text{K}$, near or beyond the vaporization temperature of most solids. Thus the dust could arise from the irradiation-driven evaporation of rocky planetesimals, analogous to the “evaporating planets” detected by *Kepler* and *K2* (Rappaport et al. 2012; Sanchis-Ojeda et al. 2015). The mass in the evaporative wind has to be at least comparable to that in the dust. The mass in micron-size grains re-

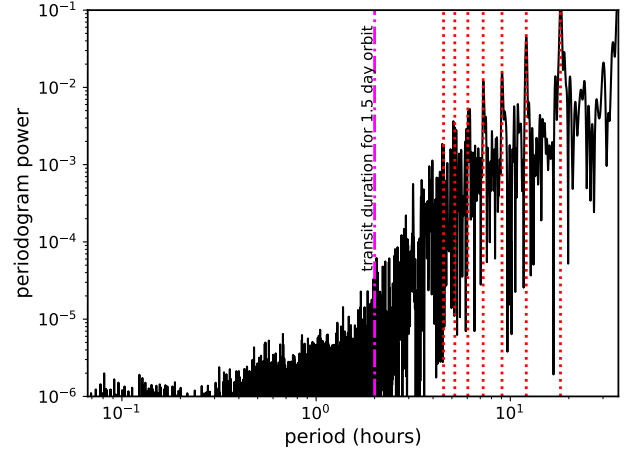


Figure 19. Periodogram of the HD 240779 lightcurve between the Nyquist limit (4 min) and the 1.51-day period of the dip signal. The expected 2-hour maximum transit duration of a small body on a circular 1.51 day around HD 240779 is marked as the vertical magenta dash-dot line. Vertical red dotted lines mark harmonics of 1.51 days.

quired to occult 10% of the disk of the star is about $4 \times 10^{14} \text{ kg}$, equivalent to a body several km across. Given the rapid changes in dip shape, the dispersal time must be of order a few orbits; replenishment by evaporation would require $\sim 10^{15} - 10^{16} \text{ W}$, far more than available by irradiation of such a body. However, energy-limited evaporation of a larger ($\gtrsim 100 \text{ km}$) body could supply the material, albeit only for a few decades to centuries before its complete destruction.

Although the dust producing the dips is not responsible for the *WISE*-detected infrared excess, the fact that these two short-lived phenomena occur simultaneously around HD 240779 – but not BD+10 714B – suggests that they are causally related. One scenario is that a perturber has excited planetesimals from a disk onto eccentric, crossing orbits where they collide and produce the dust at $\sim 0.5 \text{ AU}$ and bring them close to HD 240779, where their orbits can be circularized by non-gravitational forces. The stellar companion BD+10 714B could be this perturber, especially if the periastron is as small as 100 AU (Fig. 9). If a primordial disk is inclined by more than 40 deg. to the plane of the binary orbit, the Kozai-Lidov mechanism can act to send planetesimals on highly eccentric, highly inclined orbits (Naoz 2016). For a stellar semi-major axis of 1000 AU, planetesimals on initially circular orbits as close as a few AU and as far as a few tens of AU will experience Kozai-Lidov oscillations and could be placed on “star-grazing” orbits at the present epoch; for objects on smaller orbits, post-Newtonian precession dampens the oscillation; the shorter oscillation times for planetesimals on wider orbits mean that they would have already been destroyed (Naoz 2016).

Future work could include sub-mm observations of HD 240779 to constrain the flux at longer wavelengths and possibly to resolve any outer disk and determine its inclination, precise RV measurements to obtain the acceleration of the stars and better constrain the orbit and hence periastron and the dynamical impact on the disk, and observa-

tions of dips at multiple wavelength to detect the expected wavelength-dependent scattering indicative of dust.

ACKNOWLEDGEMENTS

The authors thank Jonathan Gagné for discussion of young moving group identifications. TJ and DL gratefully acknowledge Allan R. Schmitt for making his light curve-examining software LcTools freely available. This paper includes data collected by the *TESS* mission and archived by the Mikulski Archive for Space Telescopes at the Space Telescope Science Institute. Funding for *TESS* is provided by the NASA Explorer Program. We acknowledge support by the NASA High-End Computing (HEC) Program through the NASA Advanced Supercomputing Division at Ames Research Center for the production of the SPOC data products. Some of the data presented herein were obtained at the W. M. Keck Observatory, which is operated as a scientific partnership among the California Institute of Technology, the University of California and the National Aeronautics and Space Administration. The Observatory was made possible by the generous financial support of the W. M. Keck Foundation. This research has made use of the NASA/ IPAC Infrared Science Archive, which is operated by the Jet Propulsion Laboratory, California Institute of Technology, under contract with the National Aeronautics and Space Administration.

REFERENCES

- Adams J. D., Stauffer J. R., Monet D. G., Skrutskie M. F., Beichman C. A., 2001, *AJ*, 121, 2053
- Alencar S. H. P., et al., 2010, *A&A*, 519, A88
- Ammler-von Eiff M., Guenther E. W., 2009, *A&A*, 508, 677
- Ansdell M., Gaidos E., Williams J. P., Kennedy G., Wyatt M. C., LaCourse D. M., Jacobs T. L., Mann A. W., 2016a, *MNRAS*, 462, L101
- Ansdell M., et al., 2016b, *ApJ*, 816, 69
- Ansdell M., et al., 2019, *MNRAS*, 483, 3579
- Barenfeld S. A., Bubar E. J., Mamajek E. E., Young P. A., 2013, *ApJ*, 766, 6
- Battams K., Knight M. M., 2017, *Philosophical Transactions of the Royal Society of London Series A*, 375, 20160257
- Berger T. A., Howard A. W., Boesgaard A. M., 2018, *ApJ*, 855, 115
- Bianchi L., Shiao B., Thilker D., 2017, *ApJS*, 230, 24
- Blunt S., et al., 2017, *AJ*, 153, 229
- Bodman E. H. L., et al., 2017, *MNRAS*, 470, 202
- Bouvier J., et al., 1999, *A&A*, 349, 619
- Bouvier J., Grankin K., Ellerbroek L. E., Bouy H., Barrado D., 2013, *A&A*, 557, A77
- Bouvier J., Matt S. P., Mohanty S., Scholz A., Stassun K. G., Zanni C., 2014, *Protostars and Planets VI*, pp 433–450
- Bouvier J., et al., 2018, *A&A*, 613, A63
- Boyajian T. S., et al., 2016, *MNRAS*, 457, 3988
- Carry B., 2012, *Planet. Space Sci.*, 73, 98
- Cody A. M., Hillenbrand L. A., 2018, *AJ*, 156, 71
- Cody A. M., et al., 2014, *AJ*, 147, 82
- Curtis J. L., Agüeros M. A., Mamajek E. E., Wright J. T., Cummings J. D., 2019, *arXiv e-prints*, p. arXiv:1905.10588
- Cutri R. M., et al., 2013, Technical report, Explanatory Supplement to the AllWISE Data Release Products
- Davies C. L., Kreplin A., Kluska J., Hone E., Kraus S., 2018a, *MNRAS*, 474, 5406
- Davies C. L., et al., 2018b, *ApJ*, 866, 23
- Ellerbroek L. E., et al., 2014, *A&A*, 563, A87
- Faherty J. K., Bochanski J. J., Gagné J., Nelson O., Coker K., Smithka I., Desir D., Vasquez C., 2018, *ApJ*, 863, 91
- Fang X.-S., Zhao G., Zhao J.-K., Bharat Kumar Y., 2018, *MNRAS*, 476, 908
- Fernandes R. B., et al., 2018, *ApJ*, 856, 103
- Findeisen K., Hillenbrand L., Ofek E., Levitan D., Sesar B., Laher R., Surace J., 2013, *ApJ*, 768, 93
- Gagné J., et al., 2018, *ApJ*, 856, 23
- Gaidos E., et al., 2017, *MNRAS*, 464, 850
- Green G. M., et al., 2018, *MNRAS*, 478, 651
- Grinin V. P., Potravnov I. S., Musaev F. A., 2010, *A&A*, 524, A8
- Herbst W., Herbst D. K., Grossman E. J., Weinstein D., 1994, *AJ*, 108, 1906
- Herbst W., LeDuc K., Hamilton C. M., Winn J. N., Ibrahimov M., Mundt R., Johns-Krull C. M., 2010, *AJ*, 140, 2025
- Howard A. W., et al., 2010, *ApJ*, 721, 1467
- Huber D., et al., 2017, *ApJ*, 844, 102
- Hughes A. M., Duchêne G., Matthews B. C., 2018, *ARA&A*, 56, 541
- Husser T.-O., Wende-von Berg S., Dreizler S., Homeier D., Reinert A., Barman T., Hauschildt P. H., 2013, *A&A*, 553, A6
- Jenkins J. M., et al., 2016, in *Software and Cyberinfrastructure for Astronomy IV*. p. 99133E, doi:10.1117/12.2233418
- Jian M., Gao S., Zhao H., Jiang B., 2017, *AJ*, 153, 5
- Johnson B. C., et al., 2012, *ApJ*, 761, 45
- Jones G. H., et al., 2018, *Space Sci. Rev.*, 214, 20
- Joy A. H., 1945, *ApJ*, 102, 168
- Kennedy G. M., Wyatt M. C., 2013, *MNRAS*, 433, 2334
- Kennedy G. M., Kenworthy M. A., Pepper J., Rodriguez J. E., Siverd R. J., Stassun K. G., Wyatt M. C., 2017, *Royal Society Open Science*, 4, 160652
- Kipping D. M., Schmitt A. R., Huang X., Torres G., Nesvorný D., Buchhave L. A., Hartman J., Bakos G. Á., 2015, *ApJ*, 813, 14
- Lindgren L., et al., 2018, preprint, (arXiv:1804.09366)
- Loomis R. A., Öberg K. I., Andrews S. M., MacGregor M. A., 2017, *ApJ*, 840, 23
- Luhman K. L., Stauffer J. R., Mamajek E. E., 2005, *ApJ*, 628, L69
- Mamajek E. E., Hillenbrand L. A., 2008, *ApJ*, 687, 1264
- Mann A. W., von Braun K., 2015, *PASP*, 127, 102
- Mayama S., et al., 2018, *ApJ*, 868, L3
- McCarthy K., Wilhelm R. J., 2014, *AJ*, 148, 70
- Mentuch E., Brandeker A., van Kerkwijk M. H., Jayawardhana R., Hauschildt P. H., 2008, *ApJ*, 689, 1127
- Montiel E. J., Clayton G. C., Sugerman B. E. K., Evans A., Garcia-Hernández D. A., Kameswara Rao N., Matsuura M., Tisserand P., 2018, *AJ*, 156, 148
- Morales-Calderón M., et al., 2011, *ApJ*, 733, 50
- Morbidelli A., Raymond S. N., 2016, *Journal of Geophysical Research (Planets)*, 121, 1962
- Naoz S., 2016, *ARA&A*, 54, 441
- Natta A., Grinin V. P., Mannings V., Ungerechts H., 1997, *ApJ*, 491, 885
- Noyes R. W., Hartmann L. W., Baliunas S. L., Duncan D. K., Vaughan A. H., 1984, *ApJ*, 279, 763
- Ortega V. G., Jilinski E., de La Reza R., Bazzanella B., 2007, *MNRAS*, 377, 441
- Pearce L. A., Kraus A. L., Dupuy T. J., Ireland M. J., Rizzuto A. C., Bowler B. P., Birchall E. K., Wallace A. L., 2019, *AJ*, 157, 71
- Pecaut M. J., Mamajek E. E., 2013, *ApJS*, 208, 9
- Petigura E. A., 2015, PhD thesis, University of California, Berkeley
- Petigura E. A., et al., 2017, *AJ*, 154, 107
- Punzi K. M., Kastner J. H., Melis C., Zuckerman B., Pilachowski C., Gingerich L., Knapp T., 2018, *AJ*, 155, 33

- Rappaport S., et al., 2012, ApJ, 752, 1
- Rappaport S., et al., 2018, MNRAS, 474, 1453
- Rebull L. M., et al., 2016, AJ, 152, 113
- Ricker G. R., et al., 2014, in Space Telescopes and Instrumentation 2014: Optical, Infrared, and Millimeter Wave. p. 914320 ([arXiv:1406.0151](#)), doi:10.1117/12.2063489
- Sanchis-Ojeda R., et al., 2015, ApJ, 812, 112
- Scargle J. D., 1982, ApJ, 263, 835
- Stassun K. G., et al., 2018, AJ, 156, 102
- Stauffer J., et al., 2015, AJ, 149, 130
- Stauffer J., et al., 2018, AJ, 155, 63
- Su K. Y. L., et al., 2019, AJ, 157, 202
- Tang S.-Y., et al., 2019, ApJ, 877, 12
- Torres C. A. O., Quast G. R., da Silva L., de La Reza R., Melo C. H. F., Sterzik M., 2006, A&A, 460, 695
- Vanderburg A., et al., 2015, Nature, 526, 546
- Varga J., et al., 2017, A&A, 604, A84
- Vogt S. S., et al., 1994, in Crawford D. L., Craine E. R., eds, Proc. SPIE Vol. 2198, Instrumentation in Astronomy VIII. p. 362, doi:10.1117/12.176725
- Vural J., et al., 2014, A&A, 564, A118
- Waters C. Z., Hollek J. K., 2013, PASP, 125, 1164
- Wright J. T., Marcy G. W., Butler R. P., Vogt S. S., 2004, ApJS, 152, 261
- Wyatt M. C., van Lieshout R., Kennedy G. M., Boyajian T. S., 2018, MNRAS, 473, 5286
- Yee S. W., Petigura E. A., von Braun K., 2017, ApJ, 836, 77
- Zhan Z., et al., 2019, ApJ, 876, 127
- Zieba S., Zwintz K., Kenworthy M. A., Kennedy G. M., 2019, arXiv e-prints, p. [arXiv:1903.11071](#)
- de Wit W. J., Grinin V. P., Potravnov I. S., Shakhovskoi D. N., Müller A., Moerchen M., 2013, A&A, 553, L1

This paper has been typeset from a $\text{\TeX}/\text{\LaTeX}$ file prepared by the author.